Combustion-relevant aerosol phosphor thermometry imaging using Ce,Pr:LuAG, Ce:$GdPO_4$, and Ce:CSSO

Joshua M. Herzog[a,*], Dustin Witkowski[a], David A. Rothamer[a]

[a] *University of Wisconsin-Madison, Department of Mechanical Engineering, 1500 Engineering Dr., Madison, WI 53706, USA*

Abstract

Aerosol phosphor thermometry (APT) is a promising temperature-imaging diagnostic that is currently being developed for combustion applications. To date, gas-phase APT measurements have been limited to temperatures below 1000 K due to thermal quenching and poor sensitivity at high temperatures. In this work, three phosphor compositions are investigated for application at flame relevant temperatures: Ce,Pr:LuAG, Ce:$GdPO_4$, and Ce:CSSO. The phosphors were characterized in a temperature-controlled furnace, and measurements of gas temperature were performed in a seeded air jet after mixing with the products of an atmospheric methane-air flame. Furnace and flame measurements demonstrate that two of the phosphors are capable of temperature imaging at over 1000 K, with an upper temperature limit of at least 1400 K. Temperature precision estimates indicate 20-K or better single-shot precision from 500 to 1300 K for a seeding density corresponding to an added heat capacity of less than 1% of that of air at 1200 K at a spatial resolution of 1.12 line pairs per millimeter. This work represents the highest reported temperature measurements made using any APT technique for gas temperature measurements, and represents the highest measured quenching temperature of any phosphor exhibiting fast allowed emission for APT. These results extend the capabilities of APT for single-shot gas-phase temperature imaging up to at least 1400 K. This new capability will allow APT to be applied in combustion environments to study problems such as low-temperature ignition in engines.

*Corresponding author: jherzog2@wisc.edu
Email addresses: jherzog2@wisc.edu (Joshua M. Herzog), witkowski@wisc.edu (Dustin Witkowski), rothamer@wisc.edu (David A. Rothamer)

Keywords: aerosol phosphor thermometry (APT), thermographic phosphors, temperature measurement, particle-image velocimetry (PIV)

1. Introduction

Aerosol phosphor thermometry (APT) uses the temperature-dependent emission properties of thermographic phosphor particles to make gas temperature measurements. They are often composed of rare-earth elements doped into crystalline hosts that are ground or formed into particles (typically 0.1 to 10 μm in diameter). Seeding these particles into the flow of interest enables minimally-intrusive simultaneous planar measurements of velocity and temperature [1], making APT promising for studying turbulence-chemistry interactions in combustion devices. Unfortunately, the combination of decreasing sensitivity and signal at elevated temperatures (thermal quenching) has limited high-precision single-shot measurements to ∼900 K [2], with the highest temperature measured using APT <1000 K [3] (phosphor surface temperature measurements can range from 4-1970 K [4]). This has resulted in limited application of APT to combustion-relevant flows. See [2] for a review of the current state-of-the-art for APT.

To address these limitations, two of the Authors have analyzed the thermal quenching of rare-earth doped phosphors exhibiting allowed $4f^{N-1}5d \rightarrow 4f^N$ dipole transitions (radiative lifetimes ∼20 ns to 1 μs) [5] and have developed two new methods of obtaining high-sensitivity at elevated temperatures (co-doped APT [6] and scattering-referenced APT (SRAPT) [7]) by relying on the temperature-dependence of the phosphor's signal intensity [6, 7, 8]. In doing so, good single-shot measurement precision has been demonstrated from 300 to 900 K by tailoring the selection of phosphor and thermometry technique for the temperature range of interest [6, 8].

The goal of this work is to apply the newly developed thermometry methods to three new phosphors and extend the current measurement capabilities of APT to flame-relevant conditions ($T > 1000$ K). Each phosphor uses at least one of the new signal-based methods. Two of the phosphors (Ce:$GdPO_4$ and Ce:CSSO) are high-quenching-temperature materials not previously investigated for APT or surface temperature measurement. Each phosphors' quenching behavior and emission spectra were evaluated in

a tube furnace. Heat capacity measurements are presented in an effort to quantify one aspect of intrusiveness. Imaging measurements were performed in an air jet at room temperature (294 K) and after mixing with the products of a premixed methane flat flame. The high-temperature jet imaging measurements are compared to thermocouple measurements and used to assess the range where precise measurements are achievable. The results provide an assessment of the phosphors using the newly developed thermometry methods and the first APT measurements >1000 K.

2. APT Background

Three thermographic phosphors (Ce,Pr:LuAG, Ce:$GdPO_4$, and Ce:CSSO) were investigated in this work, each using at least one of three thermometry techniques: SRAPT, co-doped APT, and host-referenced APT. The theoretical basis for each technique has been discussed previously [6, 7, 8, 9]; a brief review is provided here. Each technique is a ratiometric diagnostic, where the ratio ($R = S_2/S_1$) is formed between a temperature-insensitive signal (S_2) and a temperature-sensitive signal (S_1). For SRAPT, S_2 is the elastically-scattered laser light signal from the seeded phosphor particles, and S_1 is luminescence emission from either Ce^{3+}, Pr^{3+}, or the host material. For co-doped and host-referenced APT, S_2 is Ce^{3+} emission, and S_1 is Pr^{3+} and host emission, respectively. Ce:$GdPO_4$ is used only for Ce^{3+} SRAPT. Ce,Pr:LuAG is used for co-doped APT, Ce^{3+} SRAPT, and Pr^{3+} SRAPT simultaneously. Similarly, Ce:CSSO is used for host-referenced APT, host SRAPT, and Ce^{3+} SRAPT simultaneously.

For each technique, the temperature precision index s_T (estimated single-shot standard deviation in temperature) can be written as (see, *e.g.,* [2])

$$s_T = \frac{s_R}{R}\frac{1}{\xi_T}, \tag{1}$$

where s_R is the precision index for the ratio, and the fractional temperature sensitivity ξ_T is defined as

$$\xi_T = \frac{1}{R}\frac{\partial R}{\partial T}. \tag{2}$$

Measurements at the highest temperatures were made for all three phosphors by employing Ce^{3+} SRAPT. In this case, the temperature-sensitivity of the signal origi-

nates from thermal quenching through nonradiative ionization of the 5d electron to the host conduction band [5], and the signal can be approximated by [10]

$$S = \frac{N_i}{1 + C_{\text{NR}} \exp\left(-\frac{\Delta E_{dc}}{k_B T}\right)}, \tag{3}$$

where N_i is the initial excited $5d$ population, C_{NR} is a temperature-independent ratio of electronic nonradiative and radiative transition probabilities, and ΔE_{dc} is the difference between the lowest Ce^{3+} $5d$ energy level and the bottom of the host conduction band.

Using Eq. 3, temperature-dependence of the SRAPT ratio, ignoring any temperature-dependence of the absorption process, is given by

$$R \propto 1 + C_{\text{NR}} \exp\left(-\frac{\Delta E_{dc}}{k_B T}\right). \tag{4}$$

Considering Eq. 1-4, one can clearly discern that the temperature at which precise measurements can be made increases with increasing ΔE_{dc}. This parameter is critical when choosing host materials for specific temperature ranges.

Figure 1 (left) displays a host-referred binding energy (HRBE) diagram for Ce^{3+} in each of the materials studied. The HRBE diagram locates the position of lowest state of the $4f^1$ (red) and $5d^1$ (blue) configurations of Ce^{3+} relative to the host bandgap. These values determine ΔE_{DC}, which is plotted in Figure 1 (right). For both Ce:$GdPO_4$ and Ce:CSSO, ΔE_{DC} is $\sim$30% larger than for Ce:LuAG, indicating that measurements can be made at higher temperatures. The high quenching temperatures for these phosphors have been partially confirmed [5, 11]. Signal-based Ce^{3+} quenching in Ce,Pr:LuAG has been observed at $\sim$800 K [8] and in Ce:$GdPO_4$ at $\sim$ 1000 K [5]. Emission lifetime data for Ce:CSSO indicate negligible thermal quenching from 300-860 K [11].

3. Experimental Methods and Materials

Three phosphors were used in this study: Ce,Pr:LuAG, Ce:CSSO, and Ce:$GdPO_4$ (Phosphor Technology, Ltd.). Table 1 lists the phosphor compositions, mean particle diameters (based on manufacturer data), mass densities (from [13]), and high-temperature heat capacity estimated from the Dulong-Petit law ($c = 3NK/M$, where

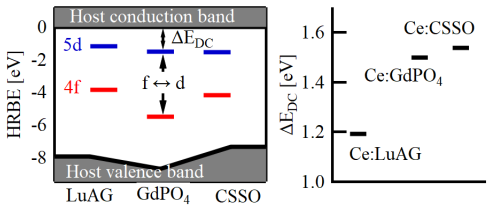

Figure 1: Host-referred binding energy diagram (left) and ΔE_{dc} for Ce,Pr:LuAG, Ce:$GdPO_4$ and Ce:CSSO (right). This diagram was constructed using the semi-empirical model developed by Dorenbos [12]. Data required to construct the diagram for Ce,Pr:LuAG, Ce:$GdPO_4$ and Ce:CSSO have been reported elsewhere [5, 11].

Table 1: Composition; mean diameter based on number ($\bar{D}_N$), area ($\bar{D}_A$), and volume ($\bar{D}_V$); mass density; particle volume; particle mass; and Dulong-Petit heat capacity ($c = 3NK/M$) for each phosphor investigated. Particle volume and mass are based on the volume-averaged diameter.

Composition	Doping [%]	$\bar{D}_N$ [μm]	$\bar{D}_A$ [μm]	$\bar{D}_V$ [μm]	Density [kg/m^3]	Volume [μm^3]	Mass [pg]	$3Nk/M$ [kJ/kg-K]
Ce,Pr:LuAG ($Lu_3Al_5O_{12}$)	0.5 ea.	0.90	0.97	1.05	6700	0.6	4.1	0.59
Ce:$GdPO_4$	0.5	1.32	1.63	2.01	5990	4.3	25.5	0.59
Ce:CSSO ($Ca_3Sc_2Si_3O_{12}$)	0.5	1.20	1.25	1.36	3510	1.3	4.6	1.02

K is the Boltzmann constant, N is the number of atoms, and M is the mass of the sample), which provides an estimate of the heat capacity in the high-temperature limit. The Ce:CSSO phosphor was annealed at 1500 K for 15 minutes with a 4 hour ramp-up and ramp-down period (rate of 300 K/hour) to reduce host defect emission that originally overlapped the Ce^{3+}spectrum. All other phosphors were used as received.

3.1. Furnace Characterization

Initial characterization of Ce:CSSO and Ce:$GdPO_4$ was performed in a tube furnace up to 1500 K. Bulk phosphor samples were placed inside the furnace in an alumina dish. The samples were excited using 266-nm (Nd:YAG 4th harmonic) laser light with a fluence of 1.5±0.3 mJ/cm^2. Spectrally-resolved emission measurements were performed using a spectrometer (Acton, SP2300i) outfitted with an intensified CCD camera (Princeton Instruments, PI-Max 4 with Gen III filmless HBf intensifier and

P46 phosphor) and a UV-rejection filter (Schott, WG-295). Temporally-resolved emission measurements were acquired with a photomultiplier (Hamamatsu, H-5783) outfitted with a UV-rejection filter (Schott WG-295). Lifetimes were extracted from the time-resolved fluorescence curves using a linear least-squares regression in log space, assuming a single exponential decay. The fit is performed starting 5 ns after the peak to avoid influence from the laser pulse, and ending after 1 decade of decay.

3.2. Heat Capacity Measurements

Heat capacity measurements for each phosphor were taken from 300-600 K with a differential scanning calorimeter (PerkinElmer, 8000 DSC) to evaluate acceptable seeding densities without appreciably increasing the heat capacity of the fluid. The scan rate was 20 K/min and a correction was applied to enforce symmetry between the heating and cooling curves. The Debye heat capacity model was fit to the data (via the Debye temperature, T_D) to extrapolate the results to higher temperatures. The measurements and extrapolation were validated by testing an aluminum oxide powder sample with known heat capacity; the deviation was $<4\%$ from the reference value [14] between 300 and 1200 K.

3.3. Flame Validation Experiment

APT flame imaging was performed in a seeded air jet (12-mm diameter) heated by a concentric flat flame (Holthuis and Associates, center tube burner). The initially unheated air jet (2 slpm) exited the center tube and mixed with the products of the methane/air flame (5.6 and 49.3 slpm flowrates for methane and air, respectively; equivalence ratio $\Phi \approx 1.1$).

The APT imaging setup, shown in Figure 2, consisted of three intensified cameras, a 10-Hz Nd:YAG laser outputting the 4$^{\text{th}}$ harmonic at 266 nm (Continuum, Powerlite 8010), and a series of sheet-forming and collection optics. The laser beam provided 10 ± 1 mJ/pulse (measured at the burner), which was formed into a laser sheet 50-mm tall and 0.8-mm thick. The laser energy was set using a variable attenuator, and the sheet was formed using a UV AR coated -75-mm FL cylindrical lens followed by a UV AR coated 500-mm FL spherical lens. The laser sheet was focused $\sim$ 50 mm

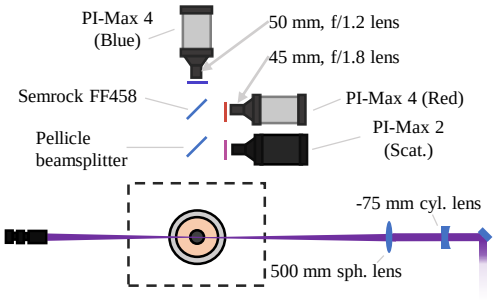

Figure 2: Experimental setup diagram for flame experiment.

Table 2: Equipment, collection efficiency $\eta_{pc}\eta_{opt}$, magnification M, and collection solid angle Ω for each band.

Band	Camera	Lens	Filters	$\eta_{PC}\eta_{opt}$ [-]	M [-]	$\Omega/4\pi$ [-]
Red	PI-Max 4	Nikon Nikkor	Reynard R00944	0.341[a]	0.17	9×10^{-4}
		50-mm ($f/1.2$)	Asahi Spectra ZVL0470	0.341[b]		
Blue	PI-Max 4	Sodern Cerco	Schott WG-295	0.144[a]	0.17	4×10^{-4}
		45-mm ($f/1.8$)	Melles Griot O3SWP604	0.180[b]		
				0.112[c]		
Scattering	PI-Max 2	100-mm singlet	Edmund 39-320	0.012	0.17	1×10^{-7}
		($f/90$)				

[a,b,c] Calculated for the Ce,Pr:LuAG (a), Ce:CSSO (b), and Ce:$GdPO_4$ (c) phosphors at 294 K.

behind the center of the tube to avoid optical breakdown. Laser fluence was estimated from Mie scattering images (at 294 K) to have a maximum value of $\sim$50 mJ/cm^2 and a mean of $\sim$30 mJ/cm^2.

Camera collection bands were chosen based on the furnace measurements. The collection efficiency at 294 K (*i.e.,* the product of photocathode quantum efficiency η_{PC} and optical transmission η_{opt} of the lens and filters, averaged over the emission spectrum) and estimated collection solid-angle Ω are provided in Table 2. Spectrally-resolved collection efficiencies are shown superimposed on the 294 K emission spectra in Figure 3. The bands used for collection are labelled "Red", "Blue", and "Scattering". A pellicle beamsplitter with $\sim$8% reflectivity was used to split off light for elastic

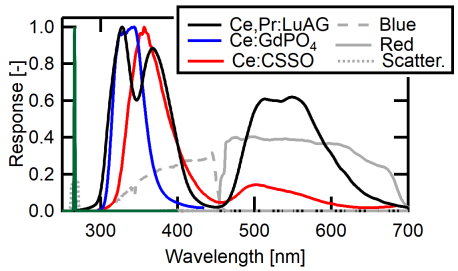

Figure 3: Emission spectra for each phosphor at 294 K with collection bands for temperature-imaging superimposed as gray lines. Spectra are normalized by their integral.

scattering measurements and was captured for all phosphors using the Scattering-band camera. Ce^{3+} emission from Ce,Pr:LuAG and Ce:CSSO was captured using the Red-band camera, whereas for Ce:$GdPO_4$ it was captured on the Blue-band camera. Pr^{3+} emission from Ce,Pr:LuAG and host emission from Ce:CSSO were captured using the Blue-band camera. The camera integration duration was fixed at 100 ns for scattering, Pr^{3+}luminescence, and Ce:$GdPO_4$ Ce^{3+}luminescence; and 200 ns for all other measurements.

Phosphor particles were seeded into the air jet using an aerosol generator (TSI, 3400A). Seeding density for Ce,Pr:LuAG was estimated based on the camera properties and previous measurements of Ce^{3+} emission intensity per particle [15]. A calibration was generated to relate elastic scattering intensity to Ce,Pr:LuAG number density. For the other phosphors, the relative scattering intensity per particle was estimated from Mie theory and used for the number density calibration. Elastic scattering intensity per particle for Ce:CSSO and Ce:$GdPO_4$ were estimated to be larger than that for Ce,Pr:LuAG by factors of 1.7 and 2.2, respectively. There is roughly a 50% uncertainty in the seeding density estimates based on uncertainties in camera parameters and scattering properties. See supplemental material for more detail.

Image data were binned using a combination of software and hardware binning (4x4 hardware binning for scattering, and 2x2 hardware followed by an additional 2x2 software binning for emission) resulting in a 0.3-mm pixel size in the object plane. Data processing included a linear registration procedure using a bicubic interpolation scheme for resampling images. Pixels with a measured emission intensity less than

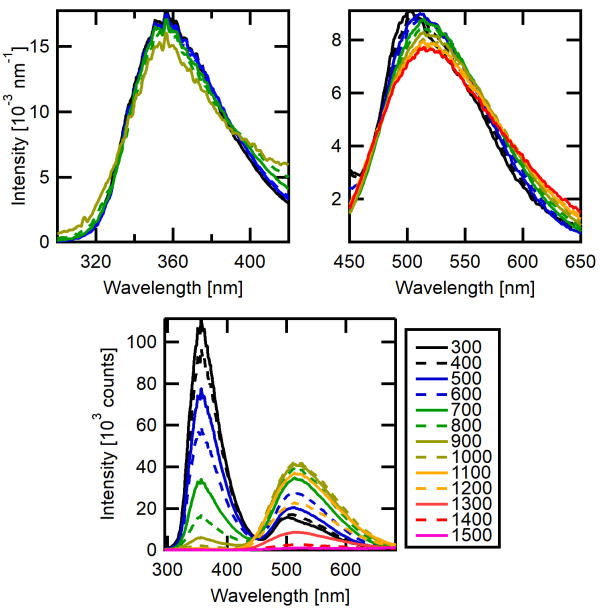

Figure 4: Emission spectra up to 1500 K for Ce:CSSO host (left) and Ce^{3+} emission (middle) normalized by their integral, and full unnormalized spectra (right).

100 counts above background, or a measured scattering intensity less than 1000 counts above background were ignored. The ratio data were filtered using a 2x2 moving-average filter resulting in an image spatial resolution of 1.12 line pairs per millimeter based on a binned and filtered image of the 1951 USAF resolution test chart (MIL-STD-150A).

Temperature profiles were measured using 0.0762-mm and 0.127-mm diameter type-R thermocouples. Three horizontal sweeps were acquired at heights above the burner (HABs) of 19, 36, and 47 mm using the 0.127-mm diameter probe. Horizontal sweeps were corrected for conduction and radiation using heat transfer and material property correlations from [16]. Temperature derivatives along the wire were determined directly from the horizontal profiles. The radiation error correction magnitude was found to vary from 10 K to 60 K (for gas temperatures of 1050 K and 1600 K, respectively), while the conduction error correction along the jet centerline varied from approximately 200 K to less than 15 K (at 600 K and 1000 K, respectively). A ver-

tical profile was taken starting at 40 mm HAB using the 0.0762-mm wire, which was corrected for radiation but not conduction, as conduction error is < 15 K for these locations.

4. Results

4.1. Furnace Characterization

Room temperature (294 K) emission spectra are shown for all phosphors in Figure 3. Ce:$GdPO_4$ emits in the near UV region at ∼320 nm with a relatively narrow bandwidth [5]. In contrast, both Ce,Pr:LuAG and Ce:CSSO have near-UV and visible emission peaks at ∼350 nm and ∼550 nm, respectively. For Ce,Pr:LuAG, the near-UV peak corresponds to Pr^{3+} emission while the visible peak corresponds to Ce^{3+} emission [15]. For Ce:CSSO, the visible peak corresponds to Ce^{3+} while the near-UV peak is believed to result from CSSO host defect emission.

The temperature dependent spectral emission characteristics of Ce,Pr:LuAG and Ce:$GdPO_4$ have been previously characterized [15, 5], so only temperature dependent spectra for Ce:CSSO are shown in Figure 4. The Ce:CSSO host emission shows almost no change in spectral shape with temperature, while the Ce:CSSO Ce^{3+} emission shows only a slight broadening and redshift of the peak (∼1.5 nm per 100 K). The emission spectra for both Ce,Pr:LuAG and Ce:$GdPO_4$ also have limited sensitivity to temperature [15, 5]. The lack of spectral sensitivity for the phosphors motivates the use of intensity-based techniques such as co-doped APT, SRAPT, and host-referenced APT.

In contrast to the emission spectra shape, the signal intensity of the phosphors shows strong temperature sensitivity as illustrated in Figure 5. Signal versus temperature was calculated from integrated emission spectra for all phosphors. Estimated quenching temperatures (T_{50}, 50% reduction in signal from peak signal) are summarized in Table 3 along with emission lifetimes (τ) at 294 K. T_{50} for Ce:CSSO is estimated based on signal from Figure 5; the remaining values were from previous studies as noted in the table. The T_{50} value for Ce:CSSO (1200 ± 100 K) is the highest reported for any thermographic phosphor utilizing $4f5d$ emission to date. The quenching

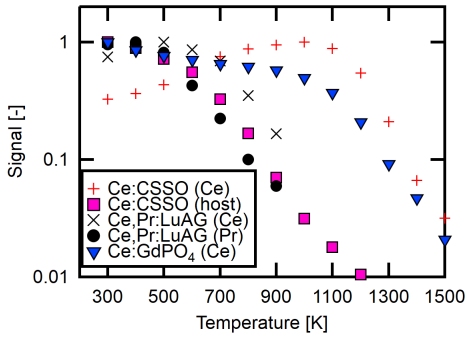

Figure 5: Relative intensity based on spectral data for all phosphors. Gd:PO_4 data is from [5] and Ce,Pr:LuAG from [15].

Table 3: 50% quenching temperature T_{50} and lifetime τ (at 294 K) of each phosphor.

Phosphor	T_{50} [K]	τ [ns]
Ce,Pr:LuAG (Ce)	800 ± 50 [15]	60
Ce,Pr:LuAG (Pr)	550 ± 50 [15]	22
Ce:CSSO (Ce)	1200 ± 100	75
Ce:CSSO (Host)	750 ± 100	43
Ce:$GdPO_4$ (Ce)	1000 ± 100 [5]	31

temperatures are found to increase with increasing ΔE_{dc}, as expected based on Eq. (3).

4.2. Phosphor Heat Capacity

Figure 6 shows heat capacity measurements for each phosphor, from 300 to 600 K, with fits to the Debye model superimposed. The theoretical Dulong-Petit heat capacity of each phosphor (last column in Table 1) agrees with the results within a few percent. These results will be used later to estimate the achievable precision for each phosphor without significantly impacting the heat capacity of the gas.

4.3. Flame Characterization

The Ce,Pr:LuAG phosphor has been characterized in depth previously [15], including the effect of laser fluence on the temperature-calibration; this calibration is

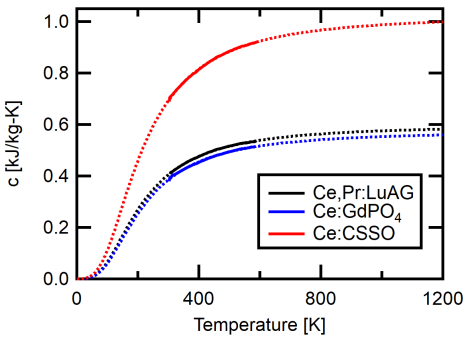

Figure 6: Heat capacity measurements for Ce,Pr:LuAG, Ce:$GdPO_4$ and Ce:CSSO, with Debye model (dotted lines).

used here. No aerosol calibration data were available for Ce:$GdPO_4$ and Ce:CSSO. Instead, an *in situ* calibration was performed using the vertical thermocouple profile for $T > 1000$ K, and the Ce,Pr:LuAG profile for $T \leq 1000$ K (Ce,Pr:LuAG temperature was used in this range due to the large conduction corrections for the thermocouple measurements). Ratio calibrations (based on fits to aerosol data) are shown in Figure 7 (left), along with the fractional temperature sensitivities (middle). The results show the high peak temperature sensitivities achievable for the intensity based methods used here.

Due to slight unsteadiness in the flame, temperature precision could not be measured directly. Instead, precision was estimated from the aerosol ratio data (Figure 7 left) along with the estimated ratio precision. At fixed laser fluence and seeding density, the temperature precision is estimated in the shot-noise limit as (see supplemental material for derivation)

$$s_T = \frac{s_R(T_0)}{R(T_0)\xi_T}\sqrt{\frac{S_1^{-1}+S_2^{-1}}{S_1^{-1}(T_0)+S_2^{-1}(T_0)}}. \tag{5}$$

where T_0 is a reference temperature (here, 294 K). The measured ratio precision at T_0 for each phosphor for the Ce^{3+}SRAPT technique is shown in Figure 8. This plot and the results of the heat capacity measurements were used to determine the value of $R(T_0)/s_R(T_0)$ for each phosphor (10, 6, and 7 for Ce,Pr:LuAG, Ce:$GdPO_4$, and Ce:CSSO, respectively, based on fits to $s_R/R = c_1 + c_2/n$ where c_1 and c_2 are the

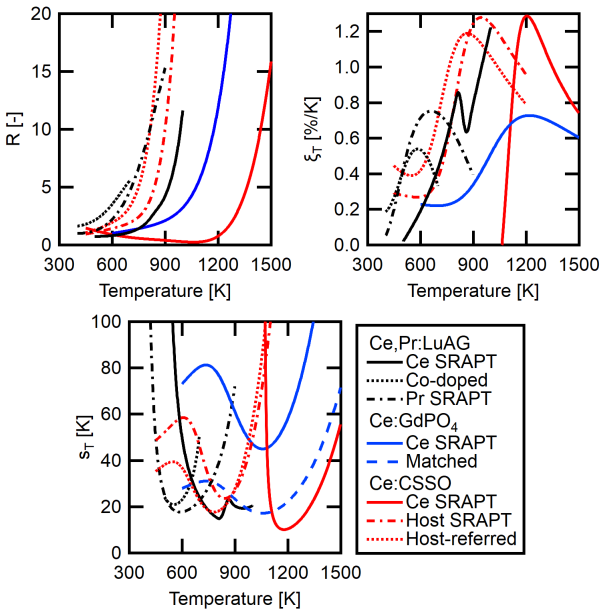

Figure 7: Ratio fit to aerosol data (Left), temperature sensitivity calculated from ratio fits (Middle), and calculated aerosol temperature-precision (Right) as a function of temperature for each technique.

fit coefficients and n is the seeding density) at a seeding density corresponding to less than 1% of the heat capacity of air at 1200 K (1000 mm^{-3} for Ce,Pr:LuAG, 220 mm^{-3} for Ce:$GdPO_4$, and 450 mm^{-3} for Ce:CSSO). The 1% limit is chosen because it is similar in magnitude to the best estimated diagnostic precision. Added heat capacity is approximately equal to the change in temperature from seeding particles into the flow; if the temperature change is interpreted as a bias, the 1% limit ensures that the bias is similar to the best-case precision.

The resulting estimates of temperature precision are shown in Figure 7 (right). Single-shot temperature precision is generally $\leq$ 20 K from 500 to 1300 K for at least one of the phosphors. Ce:$GdPO_4$ temperature precision is worse than the other phosphors due to its collection efficiency being 7$\times$ lower than Ce,Pr:LuAG (Ce^{3+}) and Ce:CSSO (Ce^{3+}) (see Table 2). The lens and image sensor used here are not optimized for UV imaging, greatly reducing the collection efficiency. To better compare Ce:$GdPO_4$'s potential performance, Figure 7 also includes an estimated temperature

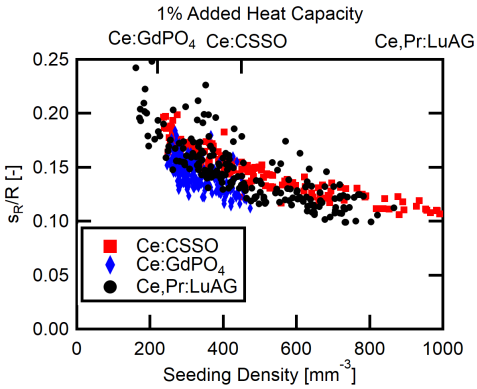

Figure 8: Measured ratio precision for the Ce^{3+} SRAPT techniques as a function of seeding density at 294 K.

precision for $Ce:GdPO_4$ with a collection efficiency equal to that of Ce:CSSO at 294 K. In this case, $Ce:GdPO_4$ is comparable with the other phosphors, with its best precision also $\sim$20 K.

Ce,Pr:LuAG performs best below 1000 K, before quenching completely. Ce:CSSO performs well throughout the entire temperature range except near 1050 K where the calibration for Ce:CSSO (Ce^{3+} SRAPT) has a local minimum. The Ce:CSSO diagnostic is expected to be best at $\sim$ 1200 K (10 K precision); $Ce:GdPO_4$ is best at $\sim$ 1050 K (45 K precision, or 17 K with matched collection efficiency).

4.4. Temperature-Imaging

A series of 200 images were taken for each phosphor at the same flame and jet conditions, with measurements starting at a HAB of 15 mm. For each phosphor, data needed for all temperature measurement methods were acquired simultaneously. Following acquisition, the data were processed separately for each phosphor and each temperature measurement method. For Ce,Pr:LuAG and Ce:CSSO this results in three temperature images: two SRAPT measurements, and one co-doped (Ce,Pr:LuAG) or host-referenced measurement (Ce:CSSO). For $Ce:GdPO_4$, a single temperature image is obtained.

For Ce,Pr:LuAG, a weighted-average temperature is calculated using the estimated temperature precision as weights (weight $w_i = 1/s_{T,i}^2$, for each method i). Tempera-

ture precision at each pixel for each measurement is estimated based on the measured temperature, ratio calibration, measured signal intensity, and manufacturer-provided camera properties.

For Ce:CSSO, the host-referenced technique is used for temperatures less than ~ 900 K where the host emission intensity is observable at the seeding densities used; host emission intensity is almost completely quenched by ~ 900 K. The Ce^{3+} SRAPT ratio for Ce:CSSO is double valued below 1100 K, and for temperatures below 1100 K the host-referenced ratio, if measureable, is used to determine which of the two temperatures is correct. If host emission is not measurable, the larger temperature determined from Ce^{3+} SRAPT is taken to be correct. This results in some additional uncertainty in absolute temperature in the temperature range from $\sim$900-1100 K. Above 1100 K, Ce^{3+} SRAPT is used. In summary, for Ce:CSSO, the host-referenced method is used exclusively where host-emission is measurable and the Ce^{3+} SRAPT method is used everywhere else.

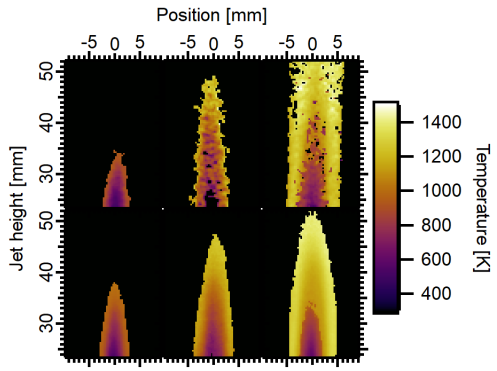

Figure 9: Single-shot (top row) and median (bottom row) temperature images from Ce,Pr:LuAG (left), Ce:$GdPO_4$ (middle), and Ce:CSSO (right) phosphors. Single-shot seeding densities (at jet center, 23 mm HAB) are 650 (Ce,Pr:LuAG), 60 (Ce:$GdPO_4$), and 130 mm^{-3} (Ce:CSSO)

Single-shot and median temperature images for each phosphor are shown in Figure 9. As seen in the images, the seeded room temperature air jet exiting the center tube is heated by the surrounding high-temperature products of the concentric methane air flat flame. The temperature range for each of the phosphors is clear by comparing the area each phosphor is able to capture, with Ce:CSSO capturing the largest temper-

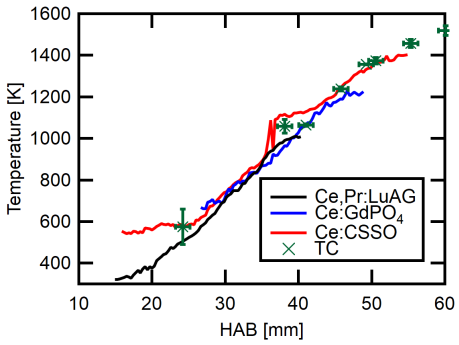

Figure 10: Median measured vertical temperature profiles for each phosphor with corrected thermocouple measurements.

ature range. At the time of writing this paper, each measurement presented meets or exceeds the highest published temperature measured using APT, with temperatures up to ∼1500 K measured on a single-shot basis using Ce:CSSO. For reference, the highest two previous APT measurements with similar single-shot precision were made up to slightly greater than 900 K [3, 7].

Median jet centerline temperature profiles for the three phosphors, along with thermocouple measurements, are shown in Figure 10. The vertical profiles show the temperature range of each phosphor (Ce,Pr:LuAG 300-1000 K, Ce:$GdPO_4$ 700-1200 K, and Ce:CSSO 500-1400 K). Good agreement (within a few percent) is generally seen between all three measurements and the thermocouple measurements. An exception to this is the jump seen in the Ce:CSSO temperature profile near 1050 K. Since host emission intensity is very low by 900 K, the host-referenced APT measurement cannot be used to reliably determine which temperature for the Ce^{3+} SRAPT calibration is correct above $\sim 900K$. In this situation, the larger temperature is assumed, biasing measurements high and resulting in steps in the profiles.

The median temperature profiles show a slightly reduced range for each phosphor compared to single-shot imaging (1400 K for CSSO and 1200 K for $GdPO_4$, compared to 1500 K and 1300 K in the single-shot images, respectively). The reduced temperature range results from slight instability in the jet mixing with the flame. Temperature fluctuations push some measurements above the phosphors' upper temperature limit,

such that only the colder fluctuations are measured reliably, biasing the median to a lower temperature. The temperature profiles tail-off at these limits as a result.

5. Conclusions

To date, APT has been limited to temperatures $<$1000 K due to thermal quenching and concomitant low sensitivity at high-temperatures. Here, three high quenching temperature phosphors have been investigated using three recently identified approaches: co-doped APT, SRAPT, and host-referenced APT [6, 7, 9]. Temperature imaging has been performed in a jet heated by mixing with the products of an atmospheric methane-air flat flame. The quenching temperature based on signal was measured for Ce:CSSO ($T_{50} = 1200 \pm 100$ K). Each of the phosphors tested is capable of measurements above 900 K. Ce,Pr:LuAG was found to be viable for APT up to $\sim$1000 K, while Ce:$GdPO_4$ and Ce:CSSO were shown to be usable up to $\sim$1200 and $\sim$1400 K, respectively. These measurements represent a significant increase in APT performance, increasing the upper temperature limit from below 1000 K to at least 1400 K. This increased temperature limit will allow APT to be applied to a range of new applications including high-precision single-shot temperature imaging of low-temperature ignition. Future work will further investigate Ce:$GdPO_4$ and Ce:CSSO in order to optimize application of APT using these phosphors.

Acknowledgments

Research was sponsored by the Army Research Office and was accomplished under Grant Number W911NF-19-1-0238. The views and conclusions contained in this document are those of the authors and should not be interpreted as representing the official policies, either expressed or implied, of the Army Research Office or the U.S. Government. The U.S. Government is authorized to reproduce and distribute reprints for Government purposes notwithstanding any copyright notation herein.

This research was partially supported by the University of Wisconsin-Madison College of Engineering Shared Research Facilities and the NSF through the Materials Science Research and Engineering Center (DMR-1720415) using instrumentation

provided at the UW-Madison Materials Science Center.

[1] A. Omrane, P. Petersson, M. Aldén, M. Linne, Simultaneous 2D flow velocity and gas temperature measurements using thermographic phosphors, Appl. Phys. B 92 (1) (2008) 99–102.

[2] C. Abram, B. Fond, F. Beyrau, Temperature measurement techniques for gas and liquid flows using thermographic phosphor tracer particles, Prog. Energy Combust. Sci. 64 (2018) 93–156.

[3] Z. Yin, B. Fond, G. Eckel, C. Abram, W. Meier, I. Boxx, F. Beyrau, Investigation of BAM:Eu^{2+} particles as a tracer for temperature imaging in flames, Combust. Flame 184 (2017) 249–251.

[4] J. Brübach, C. Pflitsch, A. Dreizler, B. Atakan, On surface temperature measurements with thermographic phosphors: a review, Prog. Energy Combust. Sci. 39 (1) (2013) 37–60.

[5] D. Witkowski, D. A. Rothamer, A methodology for identifying thermographic phosphors suitable for high-temperature gas thermometry: application to Ce^{3+} and Pr^{3+} doped oxide hosts, Appl. Phys. B 123 (8) (2017) 226.

[6] D. Witkowski, D. A. Rothamer, A novel strategy to improve the sensitivity of aerosol phosphor thermometry using co-doped phosphors, Proc. Combust. Inst. 37 (2) (2019) 1393–1400.

[7] D. Witkowski, D. A. Rothamer, Scattering referenced aerosol phosphor thermometry, Meas. Sci. Technol. 30 (4) (2019) 044003.

[8] D. Witkowski, J. Herzog, D. A. Rothamer, High-precision aerosol phosphor thermometry with Ce^{3+} and Pr^{3+} co-doped into lutetium aluminum garnet, in: 11th U.S. National Combustion Meeting, 2019.

[9] M. Dramićanin, Ž. Antić, S. Ćulubrk, S. P. Ahrenkiel, J. Nedeljković, Self-referenced luminescence thermometry with Sm^{3+} doped TiO_2 nanoparticles, Nanotechnology 25 (48) (2014) 485501.

[10] E. Nakazawa, Phosphor handbook, CRC press, 2007, Ch. 2.

[11] S. K. Sharma, Y.-C. Lin, I. Carrasco, T. Tingberg, M. Bettinelli, M. Karlsson, Weak thermal quenching of the luminescence in the $Ca_3Sc_2Si_3O_{12}$:Ce^{3+} garnet phosphor, J. Mater. Chem. C 6 (33) (2018) 8923–8933.

[12] P. Dorenbos, A review on how lanthanide impurity levels change with chemistry and structure of inorganic compounds, ECS J. Solid State Sci. Technol. 2 (2) (2013) R3001–R3011.

[13] T. Justel, Phosphor Information and Spectra Access (PISA) (2019 (accessed October 2, 2019)).
URL fh-muenster.de/ciw/personal/professoren/juestel/pisa.php

[14] D. C. Ginnings, G. T. Furukawa, Heat capacity standards for the range 14 to 1200 K., J. Am. Chem. Soc. 75 (3) (1953) 522–527.

[15] J. M. Herzog, D. Witkowski, D. A. Rothamer, Characterization of the Ce,Pr:LuAG phosphor for co-doped aerosol phosphor thermometry, in preparation.

[16] V. Hindasageri, R. Vedula, S. Prabhu, Thermocouple error correction for measuring the flame temperature with determination of emissivity and heat transfer coefficient, Rev. Sci. Instrum. 84 (2) (2013) 024902.